Computers and Fluids 156 (2017) 548–561

Contents lists available at ScienceDirect

Computers and Fluids

journal homepage: www.elsevier.com/locate/compfluid

Benchmark solutions

Simulations of viscoelastic two-phase flows in complex geometries

Hadi Zolfaghari[1], Daulet Izbassarov, Metin Muradoglu*

Department of Mechanical Engineering, Koc University, Rumelifeneri Yolu, 34450 Sariyer, Istanbul, Turkey

ARTICLE INFO

Article history:
Received 15 January 2017
Revised 22 May 2017
Accepted 27 May 2017
Available online 29 May 2017

Keywords:
Viscoelastic two-phase flow
Complex geometry
Immersed boundary method
Front-tracking method

ABSTRACT

A front-tracking/immersed-boundary (FT/IB) method is developed for direct numerical simulations of viscoelastic two-phase flow systems in complex geometries. One set of governing equations is written for the whole computational domain and different phases are treated as a single fluid with variable material and rheological properties. The interface is tracked explicitly using a Lagrangian grid while the flow equations are solved on a fixed Eulerian grid. An immersed boundary method is used to impose the boundary conditions on arbitrarily-shaped solid walls. The surface tension is computed at the interface using the Lagrangian grid and included into the momentum equations as a body force. The viscoelasticity is accounted for using the FENE-CR model. The viscoelastic model equations are solved fully coupled with the flow equations within the front-tracking framework. The FT/IB method is first validated for a single-phase and a two-phase Newtonian flow problems. Then it is applied to study motion and deformation of a viscoelastic drop in a pressure-driven flow through a capillary tube with a smooth and a sharp-edged constrictions. It is shown that the FT/IB method is robust, second order accurate in space and suitable to simulate viscoelastic two-phase flows interacting with a complex geometry.

1. Introduction

Multiphase flows interacting with complex geometries are ubiquitous in a wide range of scientific and engineering applications such as microfluidic processes [2,22,23,47], biological cells in microcirculation [12,21,56,59], emulsions and particle-laden flows in colloids and interface science [46,48] and hydrocarbon recovery processes [38,54]. Viscoelasticity plays a significant role in these applications often in the presence of confinement. In particular, viscoelasticity can be used to manipulate multiphase flows in microfluidics for various unconventional functionalities such as synthesis of non-spherical particles [10], microfluidic rectifier [17], microfluidic memory and control device [16] and enhanced mixing in microchannels [18]. Among these, viscoelastic two phase systems in complex geometries have recently gained more interest due to the outgrowth of droplet based microfluidic devices [11,13,28].

Dynamics of Newtonian two-phase systems involving complex geometries has been extensively studied both experimentally [20,39,40] and numerically [30,35,36,41,50,52]. However, effects of viscoelasticity on drop dynamics in complex geometries have received less attention and have been subject of a few experimental [5,7,26,31,40] and numerical studies [25,59,60].

The knowledge about the effects of viscoelasticity on drop dynamics in variable cross-section capillaries is incomplete and even contradictory in some cases. For example, conflicting observations have been reported about the effects of viscoelasticity on drop deformation in converging and diverging channels. Olbricht and Leal [40] studied the creeping motion of drops through a sinusoidally constricted tube. Their experimental study revealed that viscoelasticity in the matrix phase hinders the drop deformation. Chin and Han [7] and Mighri et al. [31] experimentally investigated the creeping motion of a drop in a converging conical channel. They found that the polymers in the drop phase hinder while that in the matrix enhances deformation. Later, Kim and Han [27] made similar observations in their numerical simulations. These results are consistent with the heuristic idea that viscoelasticity in dispersed/continuous phase opposes/enhances drop deformation [60]. On the other hand, computational study of Khayat [25] demonstrated that viscoelasticity in drop phase increases whereas that in the continuous phase decreases drop deformation. Zhou et al. [60] claimed to clear up these contradictory results in the literature. They numerically demonstrated that viscoelasticity in either phases may assist or impede drop deformation depending on the capillary number and the drop-to-matrix viscosity ratio. Recently, Khobdeh [26] investigated dynamics of viscoelastic two-phase systems in capillary with a periodically-varying cross-section

* Corresponding author.
E-mail addresses: mmuradoglu@ku.edu.tr, metin.muradoglu@gmail.com (M. Muradoglu).
[1] Present address: ARTORG Center, University of Bern, Bern 3010, Switzerland.

http://dx.doi.org/10.1016/j.compfluid.2017.05.026
0045-7930/

and found that viscoelasticity enhances drop deformation irrespective of which phase is viscoelastic.

Several studies have considered viscoelastic two-phase flow systems in a capillary with various contraction/expansion geometries. Harvie et al. [19] numerically studied deformation of a viscoelastic droplet moving through a planar channel with a sudden contraction/expansion. They reported qualitative agreement between the computational simulations and their own experimental results including the forked tail formation at the back of a viscoelastic droplet as it passes through the constriction. Chung et al. [8,9] numerically investigated the effects of viscoelasticity on drop dynamics in a planar sudden contraction/expansion microchannel. Their work showed that viscoelasticity enhances drop deformation and the effects are the most pronounced when it is contained in the continuous phase and viscosity ratio is high. Recently, Izbassarov and Muradoglu [22,23] have performed extensive numerical simulations to investigate the effects of viscoelasticity on drop dynamics and deformation in a capillary tube with a sudden contraction/expansion. They found that viscoelasticity interacts with drop interface in a non-monotonic and complicated way, and the two-phase viscoelastic systems exhibit very rich dynamics especially in the expansion region. More recently, Nooranidoost et al. [37] performed numerical simulations to examine effects of viscoelasticity on droplet formation in a flow focusing geometry.

In the context of the present work, the most relevant numerical studies have been done about motion of a viscoelastic droplet in a capillary tube with a smooth protrusion [3,42–45,59]. Bathe et al. [3] and Shirai et al. [43,44] subsequently used a Maxwell fluid droplet as a model for a neutrophil and studied its motion and deformation in a cylindrical capillary tube with a smooth protrusion using a finite element method. It was shown that the transit time initially increases with the shear modulus and eventually relaxes to reach a plateau as the shear modulus is further increased [3,43]. It was also found that the transit time is proportional to the viscosity of the cell and to the square root of the curvature of the constriction [43]. Later, Zhou et al. [59] investigated transit time and deformation of a neutrophil in an axisymmetric capillary tube using a Newtonian and an Oldroyd-B fluid models. Their geometry consisted of two different tubes smoothly connected by an arc of 90^o. They observed a qualitatively similar viscoelastic response as in Shirai et al. [43] and Bathe et al. [3] at moderate flow rates, i.e., the transit time decreases with viscoelasticity. However they observed that the effects of viscoelasticity are reversed when the flow rate exceeds a critical value. Recently, Shirai and Masuda [45] studied motion of a neutrophil through a rectangular channel with a moderate constriction. They found that the transit time is governed by the hydraulic diameter of the throat and the curvature of the constriction. Moreover, they suggested that a rectangular channel can be employed as a model for an axisymmetric tube with an appropriate hydraulic diameter and curvature.

Nearly all the previous studies regarding drop dynamics in a variable cross-section channels have focused on flows in a creeping flow regime. This is a limiting factor since flow is inherently unsteady and inertial effects might be important especially in severely constricted channels. In fact, the Reynolds number might be significantly larger in the constriction region resulting in significant deformation and even breakup of a droplet in constricted capillaries [23,38,41]. Izbassarov and Muradoglu [23] have recently studied the motion of pressure-driven two-phase viscoelastic systems through a constricted channel with finite Reynolds numbers but their geometry involved only sharp constrictions. They demonstrated significant influence of inertia even at moderate Reynolds numbers when the constriction is severe.

In the present work, a front-tracking/immersed-boundary (FT/IB) method is developed for direct numerical simulations of viscoelastic interfacial flow systems in a complex geometry. The method is general in the sense that viscoelasticity can exist in either or both phases with different rheological properties. However the results are presented here only for the case in which the viscoelasticity is contained in the drop phase. The fluid-solid boundary is handled using a sharp interface immersed boundary method [14,15,33], generally known as a discrete forcing approach with direct imposition of the boundary conditions [34]. Viscoelasticity is accounted for using the FENE-CR model of Chilcott and Rallison [6] but the method can accomodate virtually any version of Oldroyd-B and FENE type models [22]. The immersed boundary method is first validated for a benchmark single-phase problem, i.e., Newtonian fluid flow in a pipe with a semicircular constriction. For this case, the numerical results are compared and found to be in good agreement with the results obtained by the commercial software Fluent^{TM}. Then the method is applied to simulate the Newtonian droplet moving through a constricted tube and the results are found to be in good agreement with the computational results of Tsai and Miksis [50]. Finally the method is used to simulate more challenging cases involving motion of a viscoelastic droplet through a smoothly and a sharply constricted capillaries for a wide range of flow parameters.

2. Mathematical formulation

The flow equations are briefly presented here in the context of the front-tracking method. Following Tryggvason et al. [49] and Izbassarov and Muradoglu [22], a one field formulation is used where a single set of governing equations is written for the entire computational domain with different material properties in each phase. The surface tension is included as a body force distributed near the interface. Flow is assumed to be incompressible and material properties remain constant in each phase.

In the front-tracking framework, the mass and momentum conservation equations can be written as

$$\nabla \cdot \mathbf{u} = 0, \tag{1}$$

$$\frac{\partial \rho \mathbf{u}}{\partial t} + \nabla \cdot (\rho \mathbf{u}\mathbf{u}) = -\nabla p + \nabla \cdot \mu_s(\nabla \mathbf{u} + \nabla \mathbf{u}^T) + \nabla \cdot \boldsymbol{\tau} + \int_S \sigma \kappa \mathbf{n} \delta(\mathbf{x} - \mathbf{x_f}) dS, \tag{2}$$

where μ_s, ρ, p, $\mathbf{u}$ and $\boldsymbol{\tau}$ denote the solvent viscosity, the density, the pressure, the velocity vector and the extra stress tensor, respectively. Last term in Eq. (2) represents the body force due to the surface tension. In this term, σ, κ, $\mathbf{n}$ and S are the surface tension coefficient, twice the mean curvature, unit vector normal to the interface pointing into the drop phase and the surface area, respectively. The surface tension only acts on the interface as indicated by the three dimensional Dirac delta function, δ, whose arguments $\mathbf{x}$ and $\mathbf{x_f}$ are the points where the equation is being evaluated and an interface point, respectively.

The FENE-CR model [6] is adopted as a constitutive equation for the viscoelastic extra stresses. The model can be expressed as

$$\frac{\partial \mathbf{A}}{\partial t} + \nabla \cdot (\mathbf{u}\mathbf{A}) - (\nabla \mathbf{u})^T \cdot \mathbf{A} - \mathbf{A} \cdot \nabla \mathbf{u} = -\frac{F_A}{\lambda}(\mathbf{A} - \mathbf{I}), \tag{3}$$

$$F_A = \frac{{L_0}^2}{{L_0}^2 - \mathrm{trace}(\mathbf{A})}, \tag{4}$$

where $\mathbf{A}$, λ, L_0, F_A and $\mathbf{I}$ are the conformation tensor, the relaxation time, the extensibility parameter defined as the ratio of the length of a fully extended polymer dumbbell to its equilibrium length, the strech function and the identity tensor, respectively. The extra

stress tensor $\boldsymbol{\tau}$ is related to the conformation tensor by

$$\boldsymbol{\tau} = \frac{F_A \mu_p}{\lambda}(\mathbf{A} - \mathbf{I}), \tag{5}$$

where μ_p is the polymeric viscosity.

It is also assumed that material properties remain constant following a fluid particle, i.e.,

$$\frac{D\rho}{Dt} = 0; \quad \frac{D\mu_s}{Dt} = 0; \quad \frac{D\mu_p}{Dt} = 0; \quad \frac{D\lambda}{Dt} = 0, \tag{6}$$

where $\frac{D}{Dt} = \frac{\partial}{\partial t} + \mathbf{u}\cdot\nabla$ is the material derivative. The density, polymeric and solvent viscosities and the relaxation time vary discontinuously across the fluid interface and are specified using an indicator function ϕ as

$$\mu_p = \mu_{p,i}\phi + \mu_{p,o}(1-\phi); \ \mu_s = \mu_{s,i}\phi + \mu_{s,o}(1-\phi);$$
$$\rho = \rho_i\phi + \rho_o(1-\phi); \ \lambda = \lambda_i\phi + \lambda_o(1-\phi), \tag{7}$$

where the subscripts i and o denote the properties of the inner (dispersed) and outer (continuous) fluids, respectively. The indicator function ϕ is defined such that it is unity inside the droplet and zero outside.

3. Numerical method

The flow equations are solved fully coupled with the FENE-CR model in the framework of the front-tracking method [22]. The focus of this work is placed on a sharp interface immersed boundary algorithm and its coupling with the front-tracking method. Although it is described and implemented here for two-dimensional (axisymmetric) flows, the numerical method is general and can be readily extended to full 3D flows.

The mass and momentum conservation equations (Eqs. (1) and (2)) are solved on a staggered Cartesian grid using a projection method. The log-conformation method is used to solve the FENE-CR model equations to overcome so called high Weissenberg number problem. All the spatial derivatives are approximated using central differences except for the convective terms in the FENE-CR model for which the 5th-order WENO-Z scheme [4] is used. A time integration is done using a simple first order Euler method but second order time accuracy can be easily recovered using a predictor-corrector scheme [49]. The details of the numerical method can be found in Izbassarov and Muradoglu [22]. The method has been successfully applied to various viscoelastic two-phase flow problems [22–24,37].

3.1. Front-tracking method

The front-tracking method is briefly described here for completeness. In this approach, fluid-fluid interface is handled on a separate Lagrangian grid that consists of linked marker points moving with the local flow velocity interpolated from the Eulerian grid (Fig. 1). Each segment of Lagrangian grid between two marker points is called a front element. The surface tension is computed on the Lagrangian grid and is then distributed on the neighboring Eulerian grid points to be added to the momentum equations as a body force [49]. The indicator function is computed at each time step using the standard procedure [49] and is then employed to set the fluid properties in each phase. The Lagrangian grid is restructured at each time step by splitting very large front elements and deleting very small ones [49] to keep the front element size nearly uniform and comparable to the Eulerian grid size. Note that very small elements create unresolved wiggles while very large elements cause lack of grid resolution. Details of the front-tracking method can be found in Unverdi and Tryggvason [53] and Tryggvason et al. [49], and the treatment of viscoelasticity in Izbassarov and Muradoglu [22].

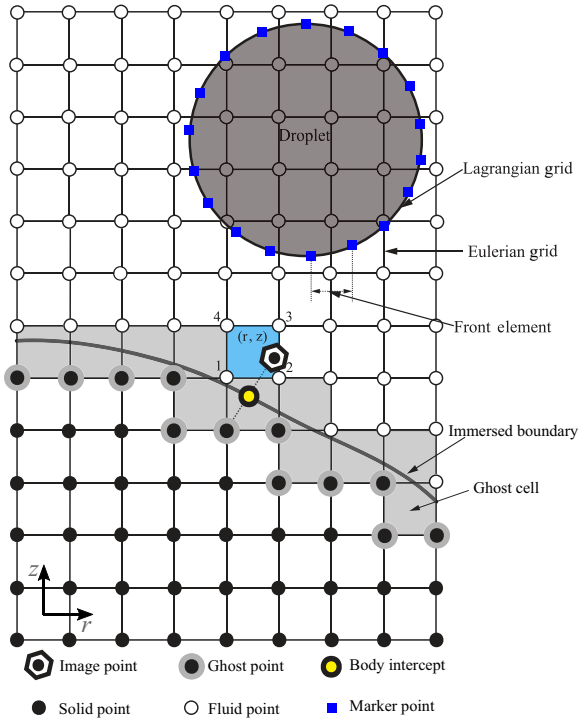

Fig. 1. The Lagrangian and Eulerian grids used in the computations. The flow equations are solved on a fixed Eulerian grid. The interface between different fluid phases is represented by a Lagrangian grid consisting of connected marker points. An immersed boundary method is applied to impose the boundary conditions on the solid boundary which cuts through the Eulerian grid. (For interpretation of the references to colour in this figure legend, the reader is referred to the web version of this article.)

3.2. Immersed boundary method

A sharp-interface immersed boundary method has been widely used to treat complex fluid-solid interfaces [34]. The present method belongs to the discrete forcing category where the immersed boundary treatment is directly applied to the discretized Navier–Stokes equations on the immersed boundaries. In this approach, an arbitrary solid surface immersed in the fluid is represented by a discrete function and the boundary conditions are imposed using the ghost cell methodology [14,15,29,33,51]. A general immersed boundary with various cell types is shown in Fig. 1. In this figure, a ghost cell (GC) is defined as an Eulerian grid cell which owns at least one solid and one fluid grid points. Similarly, a ghost point (GP) is defined as an Eulerian grid point which is in the solid region but shares a ghost cell that has at least one node in the fluid region. A ghost point is projected with respect to the solid interface to determine its associated image point (IP). The intersection point between the solid boundary and the line connecting the ghost and its associated image points is called a body intercept point (BI). A series of computational geometry operations are performed to identify the ghost points and associated image and intercept points. Since simulations are performed on a staggered grid, these operations have to be done for pressure and velocity nodes separately. However, these operations have to be performed only once prior to beginning of flow simulations.

Once the node operations are completed, we use a bilinear interpolation to determine the values of flow quantities at image points. The boundary conditions are taken into account in the interpolation process as detailed later. A given flow quantity, say ψ, is represented in the computational cell containing the image

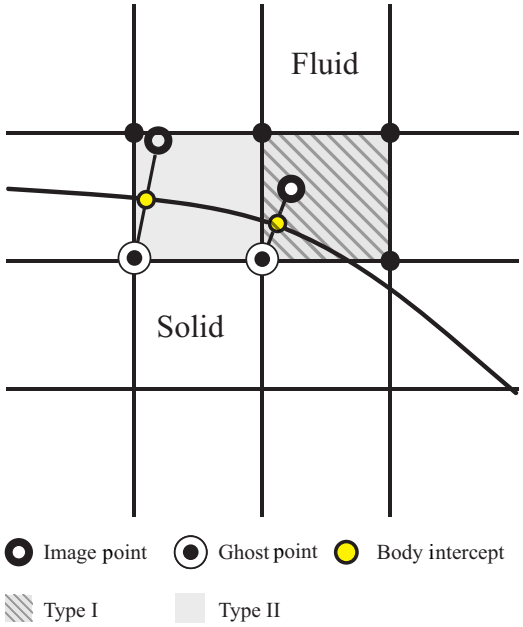

Fig. 2. The type I (cross shaded) and type II (gray colored) cells that may be encountered in the 2D image point methodology.

point as

$$\psi(r,z) = C_1 rz + C_2 r + C_3 z + C_4, \tag{8}$$

where C_i are the interpolation coefficients to be determined. In the simplest case that the cell containing the image point is completely in the fluid region as shown in Fig. 1, the coefficients can be simply computed by

$$\boldsymbol{C} = \boldsymbol{A}^{-1}\boldsymbol{\psi}, \tag{9}$$

where

$$\boldsymbol{C} = \begin{bmatrix} C_1 \\ C_2 \\ C_3 \\ C_4 \end{bmatrix}, \boldsymbol{\psi} = \begin{bmatrix} \psi_1 \\ \psi_2 \\ \psi_3 \\ \psi_4 \end{bmatrix}, \boldsymbol{A} = \begin{bmatrix} rz|_1 & r|_1 & z|_1 & 1 \\ rz|_2 & r|_2 & z|_2 & 1 \\ rz|_3 & r|_3 & z|_3 & 1 \\ rz|_4 & r|_4 & z|_4 & 1 \end{bmatrix}. \tag{10}$$

In Eq. (10), the subscripts denote the corner points of the cell (e.g., the blue shaded cell in Fig. 1). Once the vector $\boldsymbol{C}$ is determined, the value of ψ at the image point can be approximated using the bilinear interpolation as

$$[\psi]_{IP} = C_1 rz|_{IP} + C_2 r|_{IP} + C_3 z|_{IP} + C_4. \tag{11}$$

Once the image point value is estimated, the corresponding ghost point value is updated according to the Neumann or the no-slip boundary conditions for the pressure or the velocity fields, respectively. An additional treatment is needed for an image point that shares a computational cell with at least one ghost point as depicted in Fig. 2. There are two types of such cases that require special treatment in the 2D image point methodology. The type I and the type II cases involve one and two ghost points among their four neighboring nodes, respectively, as depicted in Fig. 2. Note that the three-ghost-points case is not permissible in the 2D Cartesian grid. In the type I case, the boundary conditions are readily incorporated into the interpolation procedure used to evaluate the value at the image point. For instance, in the case of a stationary wall, the no-slip boundary conditions for a velocity component on the body intercept result in

$$C_1 rz|_{BI} + C_2 r|_{BI} + C_3 z|_{BI} + C_4 = 0. \tag{12}$$

Assuming that the node 1 in Fig. 1 is the ghost point, the matrix $\boldsymbol{A}$ and vector $\boldsymbol{\psi}$ are then modified as

$$\boldsymbol{A} = \begin{pmatrix} rz|_{BI} & r|_{BI} & z|_{BI} & 1 \\ rz|_2 & r|_2 & z|_2 & 1 \\ rz|_3 & r|_3 & z|_3 & 1 \\ rz|_4 & r|_4 & z|_4 & 1 \end{pmatrix}, \boldsymbol{\psi} = \begin{bmatrix} 0 \\ \psi_2 \\ \psi_3 \\ \psi_4 \end{bmatrix}. \tag{13}$$

However, in the case of the pressure field, the Neumann boundary conditions must be applied on the solid wall, i.e., $[(\nabla p \cdot \mathbf{n})]_{wall} = 0$, where p is the pressure and $\mathbf{n}$ is the normal vector to the surface at the body intercept point. Using central differences, we obtain

$$C_1 rz|_{IP} + C_2 r|_{IP} + C_3 z|_{IP} = C_1 rz|_{GP} + C_2 r|_{GP} + C_3 z|_{GP}, \tag{14}$$

which can be re-arranged as

$$C_1(rz|_{IP} - rz|_{GP}) + C_2(r|_{IP} - r|_{GP}) + C_3(z|_{IP} - z|_{GP}) = 0. \tag{15}$$

Thus the matrix $\boldsymbol{A}$ and vector $\boldsymbol{\psi}$ become

$$\boldsymbol{A} = \begin{pmatrix} \beta_1 & \beta_2 & \beta_3 & 0 \\ rz|_2 & r|_2 & z|_2 & 1 \\ rz|_3 & r|_3 & z|_3 & 1 \\ rz|_4 & r|_4 & z|_4 & 1 \end{pmatrix}, \boldsymbol{\psi} = \begin{bmatrix} 0 \\ \psi_2 \\ \psi_3 \\ \psi_4 \end{bmatrix}, \tag{16}$$

where

$$\beta_1 = rz|_{IP} - rz|_{GP}, \ \beta_2 = r|_{IP} - r|_{GP}, \ \beta_3 = z|_{IP} - z|_{GP}. \tag{17}$$

A similar procedure can be used for the other quantities, i.e., for the extra stresses when the ambient fluid is viscoelastic. In the present study, the viscoelasticity is contained only in the drop phase which is assumed to remain distant from the solid wall at all the time.

To mitigate the problem of the type II, various approaches can be used. One straightforward methodology is to assemble the ghost point equations (including the body intercept equations for type I) into a coupled global system of linear equations. This requires solving a linear system of equations at each time step and therefore is not computationally efficient. Alternatively, the values at the type I nodes are evaluated first and then their updated values are used to convert type II cells into the type I cells which are then handled using the type I procedure. Converting type II nodes into type I nodes is done iteratively and is typically completed in a few cycles. In this way, the image point values are updated without assembling and solving an additional linear system of equations. This procedure is used in the present study and found to be highly robust and maintains overall second order accuracy of the numerical method.

4. Results and discussions

4.1. Single-phase flow

The method is first validated for a Newtonian single-phase flow in a pipe with a semicircular constriction as shown in Fig. 3. The radius of the pipe is R and the length is $L = 12R$. The radius of the constriction is $R/2$ and it is located in the middle of the pipe. The flow is assumed to be axisymmetric so a cylindrical coordinate system is adopted with z and r representing the axial and radial directions, respectively. Pressure driven flow is initiated and maintained by imposing a fully developed velocity profile at the inlet and constant pressure at the outlet. The symmetry and no-slip boundary conditions are applied at the centerline and the solid wall, respectively. For this flow, the Reynolds number is defined as $Re = \frac{\rho V R}{\mu}$ where V is the average velocity at the inlet.

Simulations are performed on a uniform Cartesian grid with grid sizes $\Delta r = R/256$ and $\Delta r = R/384$ for $Re = 1$ and $Re = 50$, respectively. Note that an unstructured triangular mesh is employed

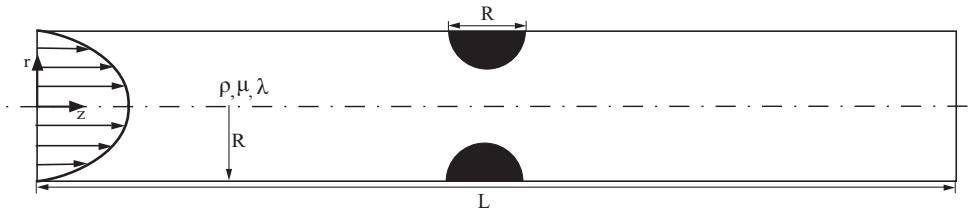

Fig. 3. The constricted pipe used for simulations of a single phase Newtonian fluid flow.

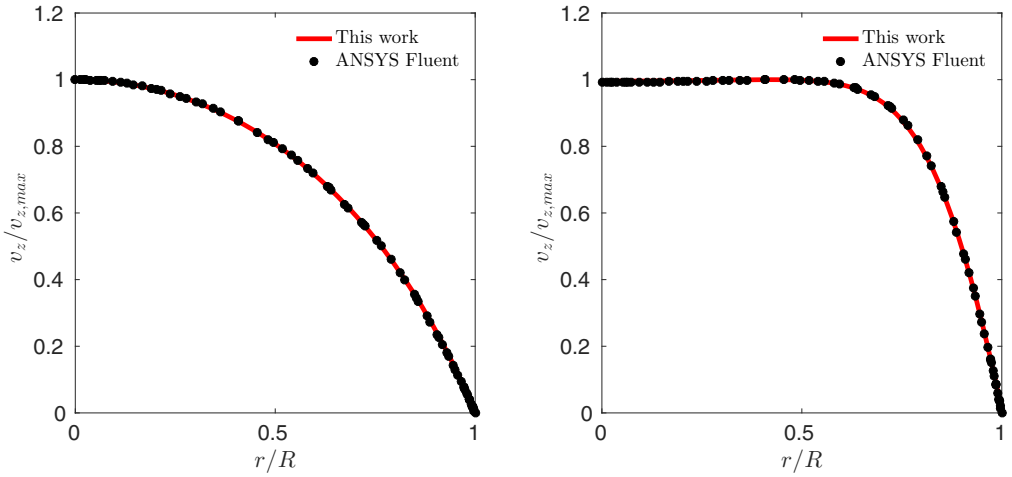

Fig. 4. The single phase Newtonian fluid flow in a pipe with a semicircular constriction on the wall. The steady state velocity profiles at the middle of the constriction for $Re = 1$ (left) and $Re = 50$ (right). The solid lines represent the present results and the symbols are the results obtained using the Fluent™ software.

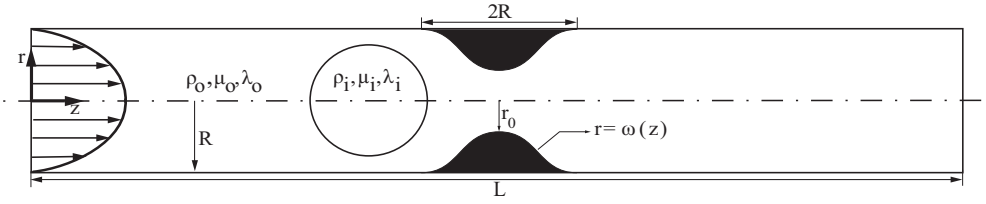

Fig. 5. The sinusoidally constricted capillary tube [50].

for the simulations in the Fluent™ software package. Fig. 4 shows the steady state velocity profiles normalized by the maximum axial velocity ($v_{z,max}$) at the neck of the constriction for $Re = 1$ and $Re = 50$. As can be seen in this figure, there is excellent agreement between the present results and the results obtained by the Fluent™ software package indicating accuracy of the immersed boundary method. Although not included in the paper, there is also good quantitative agreement between the present simulations and the results of Fluent™ software for all the flow quantities.

4.2. Multiphase flow

In this section, the method is first validated for the motion and deformation of a Newtonian droplet in a sinusoidally constricted capillary tube. This problem is selected to facilitate direct comparison of the present results with the boundary integral simulations of Tsai and Miksis [50]. Then the method is applied to study the effects of viscoelasticity on drop dynamics in two different constricted tubes.

4.2.1. Motion of a Newtonian droplet in a constricted capillary tube

This test case deals with dynamics of a Newtonian droplet in a sinusoidal constricted tube as depicted in Fig. 5. Following Tsai and Miksis [50], the constriction geometry is defined as

$$r = \omega(z) = R(1 - 0.3[1 + cos(\pi z/R)]), \quad 5R \le z \le 7R, \tag{18}$$

where R is the radius of the tube. Note that the radius of the neck is $r_0 = 0.4R$ and the length of the constriction is $2R$. A total length of the channel is $L = 12R$. A spherical droplet of radius $0.9R$ is initially located at $4R$ distance from the inlet. Flow is assumed to be axisymmetric so the symmetry boundary conditions are applied at the centerline while the no-slip boundary conditions are used on the wall. Flow is initiated instantly and maintained by imposing a fully developed velocity profile at the inlet and keeping the pressure fixed at the exit of the channel. Taking the average velocity (V) and the channel radius (R) at the inlet as the velocity and length scales, respectively, the time scale is defined as $T = \frac{R}{V}$. Following Tsai and Miksis [50], the relevant non-dimensional parameters are then defined as

$$Re = \frac{2.5\rho_o VR}{\mu_o}; Ca = \frac{\mu_o V}{\sigma}; \theta = \frac{\mu_i}{\mu_o}; \alpha = \frac{\rho_i}{\rho_o}, \tag{19}$$

where Re and Ca are the Reynolds and the capillary numbers, respectively. Note that Re in Eq. (19) corresponds to the Reynolds number at the neck. The other parameters θ and α denote the viscosity and the density ratios, respectively. Following Tsai and Miksis [50], the capillary number, and the viscosity and the density ratios are fixed at $Ca = 0.1$, $\theta = 0.01$ and $\alpha = 1$, respectively.

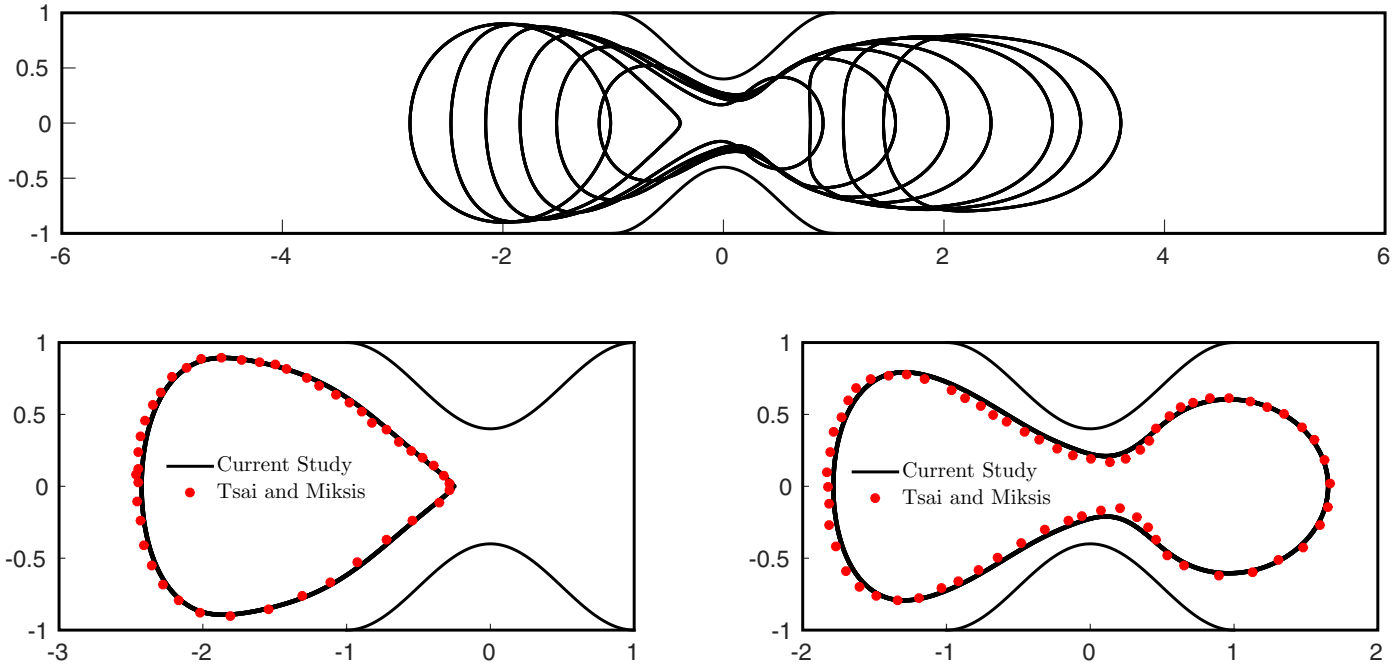

Fig. 6. Evolution of an initially spherical Newtonian droplet in a sinusoidally constricted tube. The snapshots are taken at nondimensional times of $t^* = 0$, 0.25, 0.5, 0.75, 1, 1.25, 1.5, 1.75, 2 (top row). The interface shapes are shown at nondimensional times of $t^* = 0.25$ and 0.75 (bottom row). The red symbols denote the results of Tsai and Miksis (1994) while the solid lines are the present results. ($Ca = 0.1, Re = 0.05, \theta = 0.01$ and $\alpha = 1$). (For interpretation of the references to colour in this figure legend, the reader is referred to the web version of this article.)

Although Tsai and Miksis [50] considered a creeping flow, we set $Re = 0.05$ to relax the time step restriction imposed by the numerical stability condition.

Simulations are performed using a 64×768 grid resolution. Although not shown here, this grid resolution is sufficient to obtain grid independent solutions. The top row in Fig. 6 shows the time evolution of the droplet as it passes through the constriction. As expected the droplet deforms in conformity with the shape of the constriction, i.e., the leading edge of the droplet is sharpened at the entry and the rear is flattened at the exit due to acceleration of the flow in the constriction, which is consistent with the observations of Tsai and Miksis [50]. The drop shapes are compared with the boundary integral results of Tsai and Miksis [50] in the bottom row of Fig. 6 at the nondimensional times of $t^* = 0.25$ and 0.75. As seen, the present results are in good agreement with those of Tsai and Miksis [50], illustrating the capability of the current method to accurately handle strong interactions of two-phase flows with a complex geometry.

4.2.2. A viscoelastic droplet in constricted capillaries

The method is next applied to study the dynamics of a viscoelastic droplet moving through a Newtonian liquid in two different constricted capillaries. The FENE-CR model is employed to model the viscoelasticity and the flow is considered to be axisymmetric. Thus only one half of the computational domain is used. The first capillary tube is the same as the one considered in the previous section, i.e., the sinusoidally constricted channel shown in Fig. 5. As discussed above, this geometry is motivated by the computational studies of Tsai and Miksis [50] and Udaykumar et al. [52] but they both considered only all Newtonian two-phase flow systems. To demonstrate the robustness of the numerical method, the second geometry is selected as a capillary tube with a sharp-edged protrusion as sketched in Fig. 8. The case of triangular protrusion is motivated by the computational study of Yin and Luo [57] who simulated a 2D droplet moving inside a planar microchannel with a triangular protrusion. Note that they also considered only all Newtonian two-phase flow systems. For the both cases, the constriction is placed at the middle of the channel of the radius R and length $L = 12R$. Both constrictions have the length of $2R$ and the height of $0.6R$, so the radius of the channel at the neck is $r_0 = 0.4R$. A spherical viscoelastic droplet of radius $0.7R$ is placed at the centerline with an axial distance of $4R$ from the inlet. Pressure driven flow is maintained by imposing a fully developed velocity profile at the inlet and a constant pressure at the outlet. The symmetry and no-slip boundary conditions are applied at the solid wall and the centerline, respectively.

In addition to the non-dimensional numbers defined in Eq. (19), the other relevant dimensionless parameters are the Weissenberg number $Wi = \frac{\lambda V}{R}$ and the solvent viscosity ratio $\beta = \frac{\mu_s}{\mu_s + \mu_p}$. Drop deformation parameter is defined as

$$\text{deformation} = \frac{d_a - d_r}{d_a + d_r}, \tag{20}$$

where d_a and d_r are the maximum sizes of the droplet in the axial and the radial directions, respectively. Simulations are performed for a wide range of flow parameters by changing only one parameter at a time while keeping all others fixed to demonstrate the sole effects of the parameter on the flow. To facilitate this, we define a base case as $Re = 10, Ca = 0.1, Wi = 1, \beta = 0.5, L_0 = 25, \theta = 2$ and $\alpha = 1$. Note that the base case is selected to be consistent with the range of parameters used by Izbassarov and Muradoglu [23].

Simulations are first performed to determine the grid resolution required for the grid convergence and demonstrate the second order spatial accuracy of the numerical method. For this purpose, computations are done for the base case using the grid resolutions of 64×768, 96×1152 and 128×1536, and the results are plotted in Fig. 7. As can be seen in this figure, differences between successive grid resolutions decrease as grid is refined indicating the grid convergence. The relative spatial error is also plotted in the bottom row of Fig. 7 at the selected locations indicated by the vertical dashed lines in the top row of Fig. 7. For a grid size of Δr, the

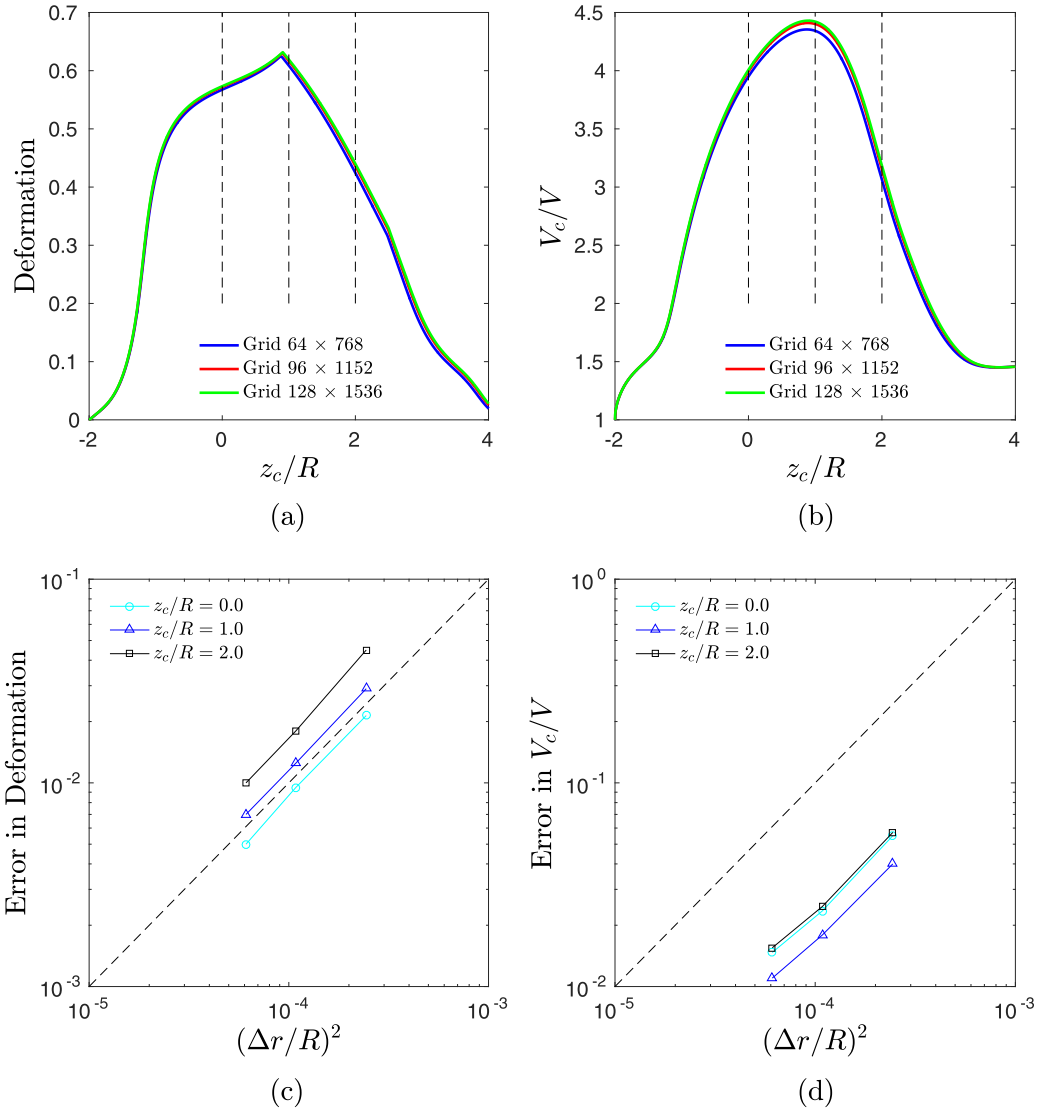

Fig. 7. Grid convergence of the numerical method for the base case. The results are obtained using various grid resolutions ranging between 64 × 768 and 128 × 1536. (a) The deformation and (b) the average axial velocity of the droplet versus the moving distance of the droplet centroid. The variation of error in (c) the deformation and (d) the average axial velocity of the droplet against the square of the non-dimensional grid size $(\Delta r/R)^2$ at the axial locations $z_c/R = 0, 1, 2$. The approximate linear relationship indicates the expected second-order accuracy of the method. ($Wi = 1$, $Re = 10$, $Ca = 0.1$, $\theta = 2$ and $\alpha = 1$).

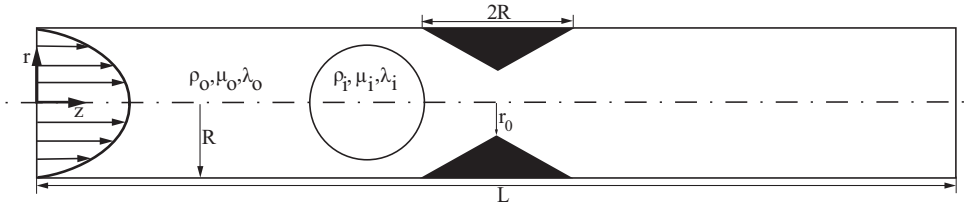

Fig. 8. The capillary tube constricted with a sharp-edged protrusion.

relative error in a flow quantity, say Q, is defined as

$$\text{Error} = \left| \frac{Q_{\Delta r \to 0} - Q_{\Delta r}}{Q_{\Delta r \to 0}} \right|, \tag{21}$$

where $Q_{\Delta r}$ is the value computed using grid resolution Δr and $Q_{\Delta r \to 0}$ is the spatial error free value predicted using the Richardson's extrapolation. The approximate linear relationship in Fig. 7 confirms the expected second order spatial accuracy of the method. The figure also shows that the 64 × 768 grid resolution is sufficient to reduce the spatial error below 5% in all the flow quantities. Therefore this grid resolution is used for all the multiphase simulations in the present study. Note that, although not shown here, the drop volume is preserved within 2% for all the cases considered in this study.

First the robustness of the present numerical method is tested. For this purpose, simulations are performed for the base case using the tubes with a sinusoidal and a sharp-edged protrusions. The evolution of the droplet in a sinusoidally constricted tube is shown in Fig. 9 where the square root of the trace of conformation tensor ($\sqrt{trace(\mathbf{A})}$) is also plotted as a measure of average polymer length. This figure shows that droplet does not deform in a full

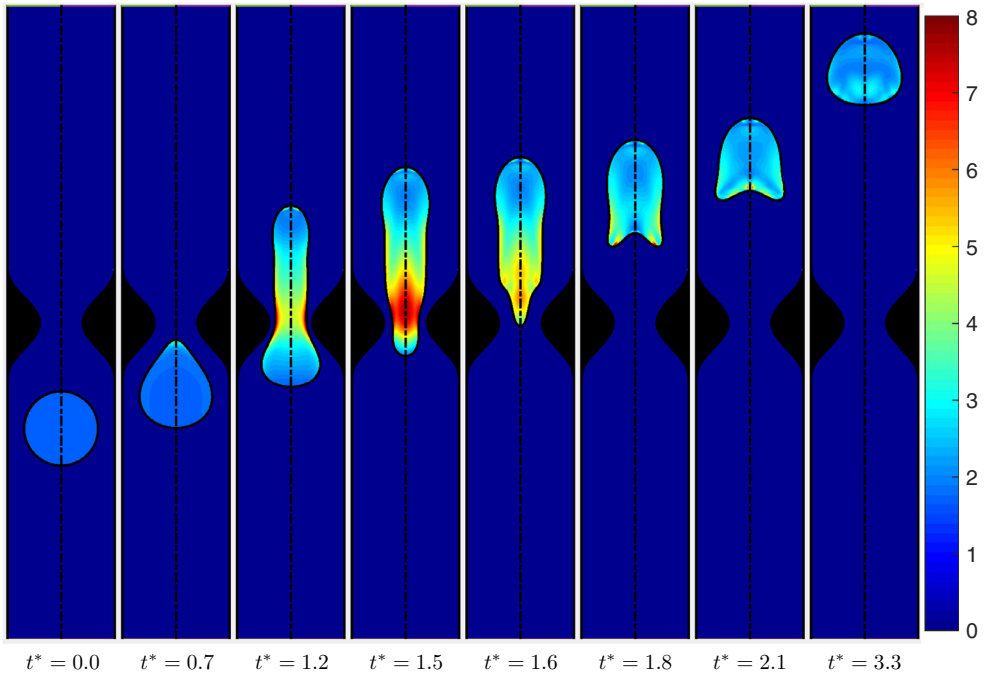

Fig. 9. Evolution of a FENE-CR droplet in a sinusoidally constricted capillary tube. Contours of average polymeric extension ($\sqrt{trace(\mathbf{A})}$) are also plotted to show the evolution of the viscoelastic stresses. ($Wi = 1$, $Re = 10$, $Ca = 0.1$, $\theta = 2$ and $\alpha = 1$, Grid: 64×768).

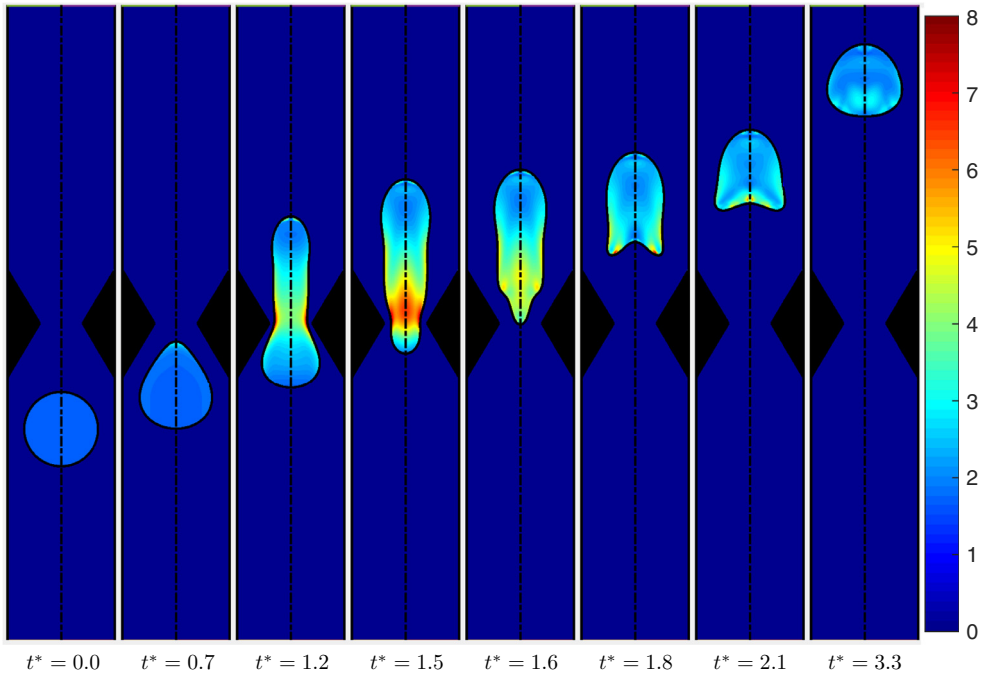

Fig. 10. Evolution of a FENE-CR droplet in a sharp-edged constricted capillary tube. Contours of average polymeric extension ($\sqrt{trace(\mathbf{A})}$) are also plotted to show the evolution of the viscoelastic stresses. ($Wi = 1$, $Re = 10$, $Ca = 0.1$, $\theta = 2$ and $\alpha = 1$, Grid: 64×768).

compliance with the shape of the constriction, which is mainly attributed to the inertial effects that are expected to be significant especially in the constriction region. As seen, the droplet elongates in the constriction and retracts back in the expansion region. The polymers in the droplet fluid undergo a strong extensional strain in the axial direction as the droplet enters the contraction. Once the droplet is within the constriction, high viscous shear stresses in the bulk fluid between the wall and the interface induce large tangential viscoelastic stresses and elongate polymers parallel to the interface as seen at $t^* = 1.2$ in Fig. 9. As the droplet moves forward, this region grows and penetrates further inside the droplet ($t^* = 1.5$). In the expansion region, the flow decelerates and the tail of the droplet retracts towards the exit of the constriction and significantly reduces the viscoelastic stresses as the polymers relax to their equilibrium length ($t^* = 1.6$). After the tail retracts, the posterior dimple occurs at the trailing edge of the droplet ($t^* = 1.8$) and the shape eventually relaxes towards a typical shape as observed in the all Newtonian systems ($t^* = 3.3$). Very similar results

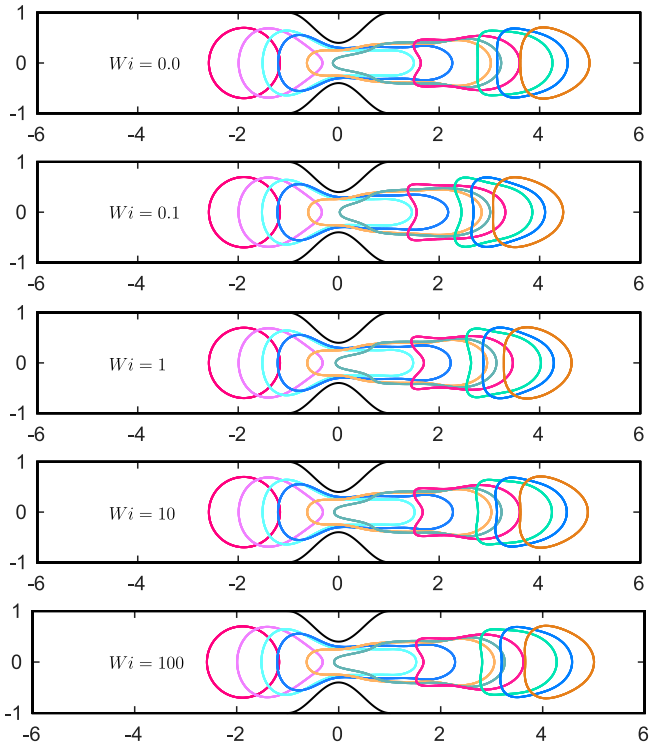

Fig. 11. Effects of viscoelasticity on dynamics of a FENE-CR droplet in the range of $Wi = 0$ (Newtonian) and $Wi = 100$ (highly viscoelastic). The snapshots are taken at $t^* = 0.0,\ 0.5,\ 0.8,\ 1.0,\ 1.3,\ 1.4,\ 1.6,\ 2.0,\ 2.2,\ 2.5$. ($Re = 10,\ Ca = 0.1,\ \theta = 2,\ \alpha = 1$, Grid: 64×768).

are also obtained for the sharp-edged protrusion case as shown in Fig. 10. The analogous results for these two different geometries are mainly attributed to the inertia which significantly suppresses effects of the shape of the constriction. These results show that the constriction geometry does not play significant role in drop dynamics for the base case. Thus only the sinusoidal constricted channel is used in the rest of the paper. However, the smooth flow field and viscoelastic stresses observed in the both cases without any sign of numerical instability indicate the robustness and accuracy of the present numerical method.

We next examine the effects of viscoelasticity on drop dynamics in the sinusoidally constricted channel. For this purpose, the Weissenberg number is varied between $Wi = 0$ (Newtonian) and $Wi = 100$ (highly viscoelastic) while keeping the other parameters the same as the base case. The shape evolution is shown in Fig. 11 for $Wi = 0, 0.1, 1, 10$ and 100 to qualitatively illustrate the effects of the viscoelasticity on the drop dynamics. This figure shows that the overall droplet evolution is not significantly affected by the Weissenberg number, i.e., the droplet deforms in the constriction, retracts in the expansion and eventually relaxes to a steady shape in the downstream of the channel for all the Weissenberg numbers. However, a close examination of Fig. 11 reveals that there is a noticeable viscoelastic effect especially in the downstream region up to $Wi = 10$. This can be better seen in Fig. 12 where the deformation and average axial velocity of the droplet are plotted as a function of the moving distance of the droplet centroid. This figure shows that the effects of the viscoelasticity are significantly more pronounced in the expansion region. In general, the droplet deformation is inhibited by the viscoelastic normal stresses in the droplet phase in a complicated and non-monotonic way. Droplet deformation decreases up to $Wi = 0.1$ and then increases to eventually relax to the all Newtonian case. This non-monotonic behavior is attributed to the fact that viscoelasticity reacts to flow with a finite time proportional to the polymer relaxation time λ, and is consistent with the numerical simulations of Zhou et al. [60] and Izbassarov and Muradoglu [22]. At low Weissenberg numbers (i.e., up to $Wi = 0.1$), the relaxation time is small. Thus less time is required to attain the maximum level of viscoelastic stresses which act to inhibit droplet deformation and droplet mobility. As Wi is further increased, there is not a sufficient time for the viscoelastic stresses to react to the flow before the droplet leaves the constriction, which reduces the effects of viscoelasticity on drop dynamics. When $Wi > 10$, the droplet behaves like a Newtonian droplet. Similar trend is also observed for the axial velocity of the droplet centroid as seen in Fig. 12. The viscoelasticity reduces droplet deformation and thus moves the interface closer to the wall, thereby leading to an overall decrease in droplet mobility. The present results are in qualitative agreement with the numerical simulations of Wu [55], Yue et al. [58], Aggarwal and Sarkar [1], and with experimental observations of Mighri et al. [32].

Simulations are then performed to examine the inertial effects on viscoelastic droplet dynamics. First the evolution of droplet shape and viscoelastic stresses are shown in Fig. 13 for $Re = 50$ and $Wi = 100$ to illustrate the combined effects of the inertia and the viscoelasticity. The other parameter are the same as in the base case. This figure shows that the droplet significantly elongates as it passes through the constriction, which is mainly attributed to effects of inertia as will be discussed below. The viscoelastic stresses are mainly generated along the interface near the wall of the constriction and quickly penetrate inside the droplet making the distribution nearly uniform in the radial direction. A bulge is formed as a result of recirculation at the leading edge of the droplet as also observed by Udaykumar et al. [52]

Next the effects of the Reynolds number are investigated. For this purpose, the Reynolds number is varied between $Re = 1$ and $Re = 50$ while keeping the other parameters the same as in the base case. The shape evolution of a droplet is plotted in Fig. 14 for $Re = 1, 10, 20$ and 50 at times $t^* = 0, 0.5, 0.8, 1, 1.3, 1.4, 1.6, 2, 2.2$ and 2.5. This figure clearly shows strong inertial effects on the drop dynamics especially in the downstream of the constriction. The droplet elongates more as the Reynolds number increases. The bulge formation occurs only at $Re = 50$. The inertial effects are quantified in Fig. 15 where the droplet deformation and the average axial velocity of the droplet are plotted against the moving distance of the droplet centroid. The results for the corresponding Newtonian droplet are also shown in Fig. 15 to highlight the effects of viscoelasticity. This figure confirms the large effects of the Reynolds number on the drop dynamics.

We finally study the effects of the capillary number on dynamics of a viscoelastic droplet. The capillary number quantifies the relative importance of the surface tension compared to the viscous stresses and droplet tends to deform more easily as the capillary number increases. The evolution of the droplet shape together with the viscoelastic stresses is shown in Fig. 16 for $Wi = 100$ and $Ca = 1$ to demonstrate the combined effects of viscoelasticity and deformability, and their interactions with the constriction. A forked tail is formed as the droplet passes through the constriction and grows further in the downstream. Note that the filament at the trailing edge is likely to rupture in the downstream of the constriction but breakup is not allowed in the present simulations. As before, the viscoelastic stresses are mainly induced near the tip of the constriction but remain concentrated at the back of the droplet due to lack of strong internal circulation in the droplet at this relatively high capillary number. Simulations are then performed for a range of capillary numbers between $Ca = 0.05$ and $Ca = 1$ while keeping the other parameters fixed at their values in the base case and results are shown in Figs. 17 and 18. Fig. 17 qualitatively shows that the droplet deformation increases with the capillary

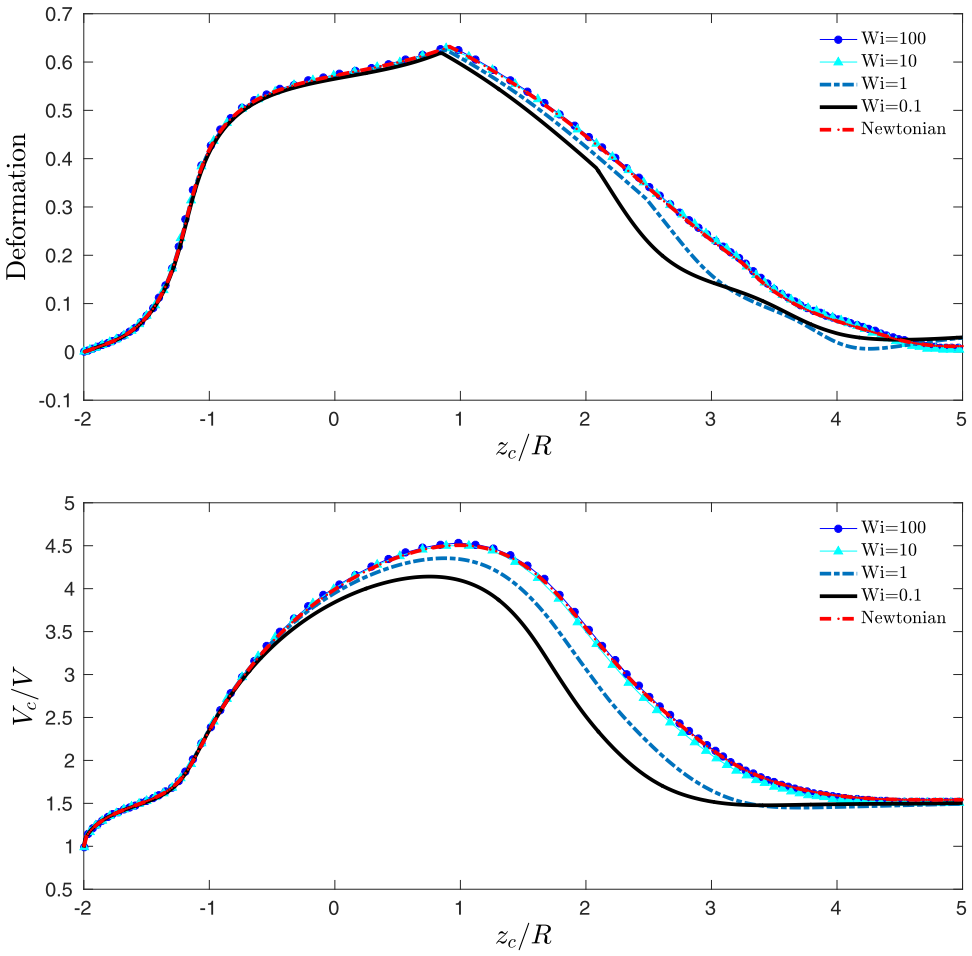

Fig. 12. Effects of viscoelasticity on dynamics of a FENE-CR droplet in the range of $Wi = 0$ (Newtonian) and $Wi = 100$ (highly viscoelastic). The deformation (upper plot) and the axial velocity (lower plot) of the droplet are plotted against the moving distance of the droplet centroid. ($Re = 10$, $Ca = 0.1$, $\theta = 2$, $\alpha = 1$, Grid: 64×768).

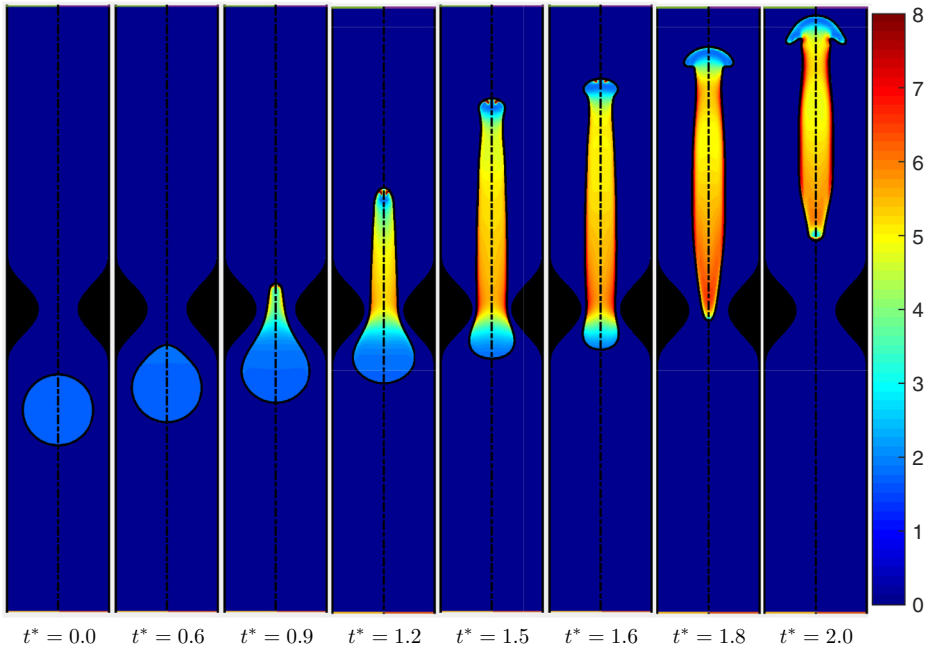

Fig. 13. Evolution of a FENE-CR droplet in a sinusoidally constricted capillary tube. Contours of average polymeric extension ($\sqrt{trace(\mathbf{A})}$) are also plotted to show the evolution of the viscoelastic stresses. ($Wi = 100$, $Re = 50$, $Ca = 0.1$, $\theta = 2$, $\alpha = 1$, Grid: 64×768).

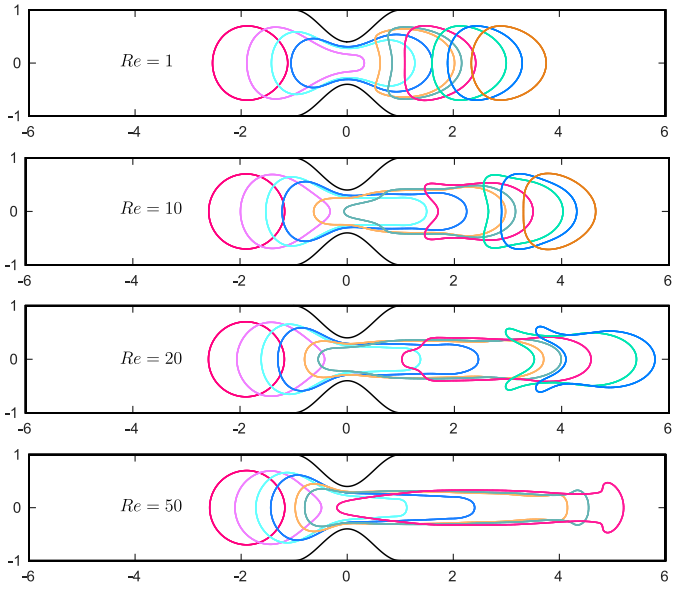

Fig. 14. Effects of Reynolds number on dynamics of a FENE-CR droplet in the range of $Re = 1$ and $Re = 50$. The snapshots are taken at $t^* = 0.0, 0.5, 0.8, 1.0, 1.3, 1.4, 1.6, 2.0, 2.2, 2.5$. ($Wi = 1$, $Ca = 0.1$, $\theta = 2$, $\alpha = 1$, Grid: 64×768).

number as expected. It also shows that the forked tail formation occurs at the trailing edge before the droplet leaves the constriction at high capillary numbers, i.e., $Ca \geq 0.5$. The effects of capillary number are quantified in Fig. 18 where the average droplet velocity and the droplet deformation are plotted as a function of the moving distance of droplet centroid. The results for the corresponding Newtonian droplet are also shown in Fig. 18 to demonstrate the effects of the viscoelasticity. This figure clearly shows the large dependence of drop dynamics on the capillary number. In the case of $Ca = 0.05$, the droplet almost completely occupies the constriction region leaving a very thin liquid film between the droplet and the solid wall. On the other hand, the droplet easily deforms and squeezes through the constriction with a relatively large liquid film between the wall and the droplet interface for $Ca = 1$. The average axial velocity increases as Ca increases since the droplet easily deforms and elongates near the centerline where flow velocity is the maximum whereas, in the case of small Ca, the droplet resists to viscous shear stresses and thus its average velocity becomes smaller. As also mentioned before, the viscoelasticity inhibits droplet deformation and thus decreases its mobility.

5. Conclusions

A sharp interface immersed boundary method has been developed and coupled with a finite-difference/front-tracking algorithm

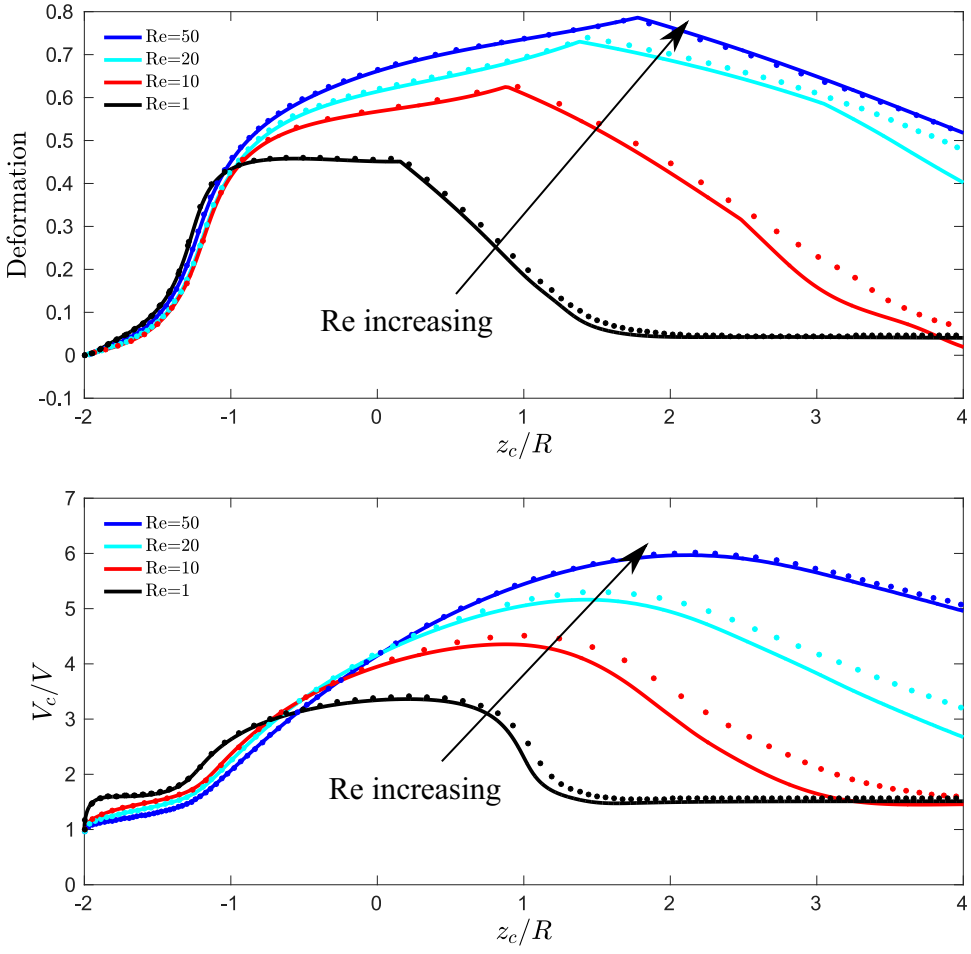

Fig. 15. Effects of Reynolds number on dynamics of a FENE-CR drolpet in the range of $Re = 1$ and $Re = 50$. The deformation (upper plot) and the average axial velocity (lower plot) of the droplet are plotted against the moving distance of the droplet centroid. The solid lines and the symbols denote the results for the viscoelastic and the corresponding Newtonian cases, respectively. ($Wi = 1$, $Ca = 0.1$, $\theta = 2$, $\alpha = 1$, Grid: 64×768).

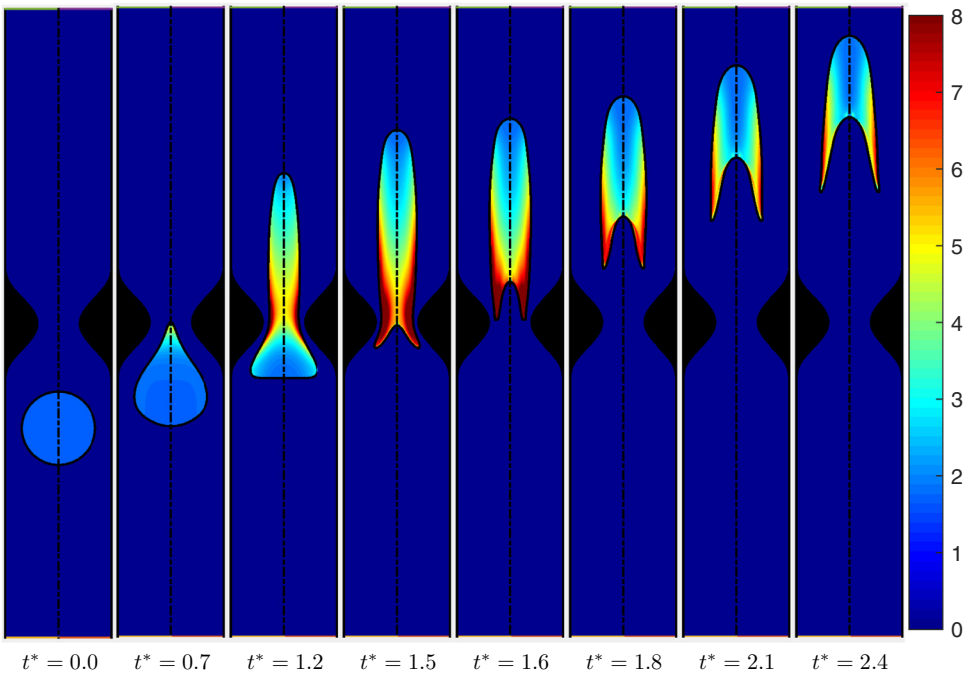

Fig. 16. Evolution of a highly viscoelastic droplet in a sinusoidally constricted capillary tube. Contours of average polymeric extension ($\sqrt{trace(\mathbf{A})}$) are also plotted to show the evolution of the viscoelastic stresses. ($Wi = 100$, $Re = 10$, $Ca = 1.0$, $\theta = 2$, $\alpha = 1$, Grid: 64×768).

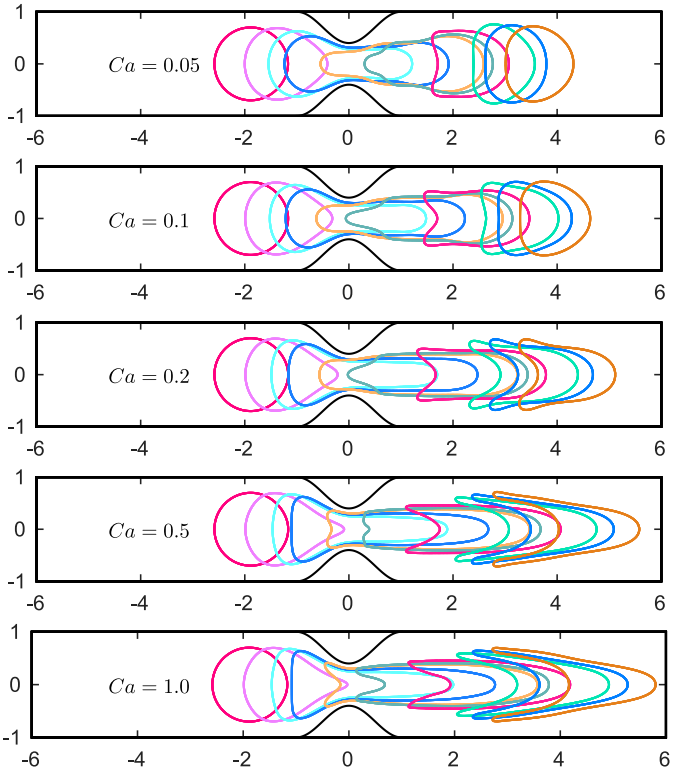

Fig. 17. Effects of capillary number on dynamics of a FENE-CR droplet in the range of $Ca = 0.05$ and $Ca = 1$. The snapshots are taken at $t^* = 0.0$, 0.5, 0.8, 1.0, 1.3, 1.4, 1.6, 2.0, 2.2, 2.5. ($Wi = 1$, $Re = 10$, $\theta = 2$, $\alpha = 1$, Grid: 64×768).

for direct numerical simulations of viscoelastic droplets moving through complex geometries. The method is general and applicable to virtually any viscoelastic multiphase flow system but it is implemented only for axisymmetric flows and the viscoelasticity is contained only in the droplet fluid in this paper. The solid boundary is represented by an arbitrary smooth function and a ghost cell methodology is used to impose the boundary conditions on the wall. A bilinear interpolation scheme is employed to approximate the boundary conditions and the method is found to be very robust and maintains the overall second order spatial accuracy of the numerical algorithm. A computational geometry procedure is developed to identify the ghost points and the associated intercept and image points. The procedure is found to be very robust and effective even for the extreme case of a sharp-edged protrusion.

The immersed boundary method is first validated for a single and a multiphase benchmark cases. The method is then applied to study the effects of viscoelasticity on droplet dynamics in a smoothly and a sharply constricted channels. The viscoelasticity is accounted for using the FENE-CR model of Chilcott and Rallison [6]. Extensive simulations are performed to examine the effects of Weissenberg, Reynolds and capillary numbers. It is found that the viscoelasticity influences the drop dynamics significantly especially in the downstream in a highly complicated and non-monotonic way. The viscoelasticity generally inhibits the droplet deformation and thus decreases its mobility. Compared to the all Newtonian case, droplet deformation decreases as Wi increases up to $Wi = 0.1$ and then relaxes back to the all Newtonian case as Wi is further increased. It is found that Reynolds number strongly influences the drop dynamics. The droplet deformation monotonically increases and the droplet elongates more along the centerline as the Reynolds number increases. A bulge formation is observed at the leading edge of the droplet at high Reynolds numbers, i.e., $Re \geq 20$. The effects of the capillary number are also examined. It is found that the droplet deformation increases as Ca increases as expected. The viscoelastic stress concentration occurs near the solid wall as the droplet passes through the constriction due to the stretching of polymers by the large velocity gradients there. A forked tail formation occurs at the back of the droplet as it passes through the constriction at high capillary numbers, i.e., $Ca \geq 0.5$.

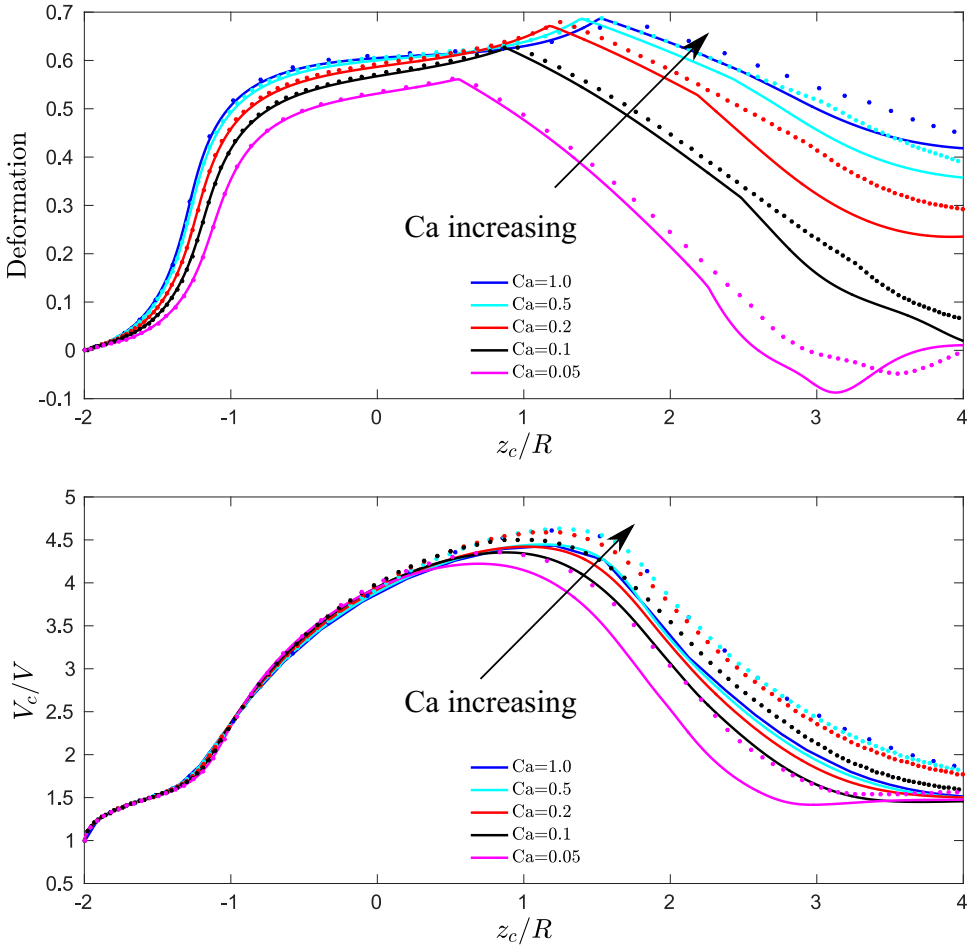

Fig. 18. Effects of capillary number on dynamics of a FENE-CR drolpet in the range of $Ca = 0.05$ and $Ca = 1$. The deformation (upper plot) and the average axial velocity (lower plot) of the droplet are plotted against the moving distance of the droplet centroid. The solid lines and the symbols denote the results for the viscoelastic and the corresponding Newtonian cases, respectively. ($Wi = 1$, $Re = 10$, $\theta = 2$, $\alpha = 1$, Grid: 64×768).

Acknowledgement

The authors are grateful to the Scientific and Technical Research Council of Turkey (TUBITAK) for the support of this research through Grant 112M181 and Turkish Academy of Sciences (TUBA).

References

[1] Aggarwal N, Sarkar K. Deformation and breakup of a viscoelastic drop in a newtonian matrix under steady shear. J Fluid Mech 2007;584:1–21.
[2] Amini H, Lee W, Carlo DD. Inertial microfluidic physics. Lab Chip 2014;14:2739–61.
[3] Bathe M, Shirai A, Doerschuk CM, Kamm RD. Neutrophil transit times through pulmonary capillaries: the effects of capillary geometry and fMLP-stimulation. Biophys J 2002;83(4):1917–33.
[4] Borges R, Carmona M, Costa B, Don WS, Comput J. An improved weighted essentially non-oscillatory scheme for hyperbolic conservation laws. J Comput Phys 2008;227:3191–211.
[5] Bourry D, Khayat RE, Utracki LA, Godbille F, Picot J, Luciani A. Extensional flow of polymeric dispersions. Polym Eng Sci 1999;39(6):1072–86.
[6] Chilcott MD, Rallison JM. Creeping flow of dilute polymer solutions past cylinders and spheres. J Non-Newtonian Fluid Mech 1988;29:381–432.
[7] Chin HB, Han CD. Studies on droplet deformation and breakup. I. Droplet deformation in extensional flow. J Rheol 1979;23(5):557–90.
[8] Chung C, Hulsen MA, Kim JM, Ahn KH, Lee SJ. Numerical study on the effect of viscoelasticity on drop deformation in simple shear and 5:1:5 planar contraction/expansion microchannel. J Non-Newtonian Fluid Mech 2008;155(1):80–93.
[9] Chung C, Kim JM, Hulsen MA, Ahn KH, Lee SJ. Effect of viscoelasticity on drop dynamics in 5:1:5 contraction/expansion microchannel flow. Chem Eng Sci 2009;64(22):4515–24.
[10] Dendukuri D, Tsoi K, Hatton TA, Doyle PS. Controlled synthesis of nonspherical microparticles using microfluidics. Langmuir 2005;21(6):2113–16.
[11] Derzsi L, Kasprzyk M, Plog JP, Garstecki P. Flow focusing with viscoelastic liquids. Phys Fluids 2013;25(9). 092001.
[12] Fauci LJ, Gueron S. Computational modeling in biological fluid dynamics, 124. New York: Springer-Verlag; 2001.
[13] Forsyth AM, Wan J, Ristenpart WD, Stone HA. The dynamic behavior of chemically stiffened red blood cells in microchannel flows. Microvasc Res 2010;80(1):37–43.
[14] Ghias R, Mittal R, Dong H. A sharp interface immersed boundary method for compressible viscous flows. J Comput Phys 2007;225(1):528–53.
[15] Ghias R, Mittal R, Lund TS. A non-body conformal grid method for simulation of compressible flows with complex immersed boundaries. AIAA paper 2004;80(2004).
[16] Groisman A, Enzelberger M, Quake SR. Microfluidic memory and control devices. Science 2003;300(5621):955–8.
[17] Groisman A, Quake SR. A microfluidic rectifier: anisotropic flow resistance at low Reynolds numbers. Phys Rev Lett 2004;92(9). 094501.
[18] Groisman A, Steinberg V. Efficient mixing at low Reynolds numbers using polymer additives. Nature 2001;410(6831):905–8.
[19] Harvie DJE, Cooper-White JJ, Davidson MR. Deformation of a viscoelastic droplet passing through a microfluidic contraction. J Non-Newtonian Fluid Mech 2008;155(1):67–79.
[20] Hemmat M, Borhan A. Buoyancy-driven motion of drops and bubbles in a periodically constricted capillary. Chem Eng Commun 1996;148–150(1):363–84.
[21] Hosseini SM, Feng JJ. A particle-based model for the transport of erythrocytes in capillaries. Chem Eng Sci 2009;64(22):4488–97.
[22] Izbassarov D, Muradoglu M. A front-tracking method for computational modeling of viscoelastic two-phase flow systems. J Non-Newtonian Fluid Mech 2015;223:122–40.
[23] Izbassarov D, Muradoglu M. A computational study of two-phase viscoelastic systems in a capillary tube with a sudden contraction/expansion. Phys Fluids 2016a;28(1). 012110.
[24] Izbassarov D, Muradoglu M. Effects of viscoelasticity on drop impact and spreading on a solid surface. Phys Rev Fluids 2016b;1(2). 023302.
[25] Khayat RE. Boundary element analysis of planar drop deformation in confined flow. Part II. Viscoelastic fluids. Eng Anal Boundary Elem 1998;22(4):291–306.

[26] Khobdeh S. Drop deformation and breakup in confined flows of viscoelastic two-phase systems. PhD thesis. Pennsylvania State University; 2011.
[27] Kim SJ, Han CD. Finite element analysis of axisymmetric creeping motion of a deformable non-newtonian drop in the entrance region of a cylindrical tube. J Rheol 2001;45(6):1279–303.
[28] Lee M, Park W, Chung C, Lim J, Kwon S, Ahn KH, et al. Multilayer deposition on patterned posts using alternating polyelectrolyte droplets in a microfluidic device. Lab Chip 2010;10:1160–6.
[29] Majumdar S, Iaccarino G, Durbin P. RANS solvers with adaptive structured boundary non-conforming grids. In: Annual research briefs, center for turbulence research, Stanford University; 2001. p. 353–466.
[30] Manga M. Dynamics of drops in branched tubes. J Fluid Mech 1996;315:105–17.
[31] Mighri F, Ajji A, Carreau PJ. Influence of elastic properties on drop deformation in elongational flow. J Rheol 1997;41(5).
[32] Mighri F, Carreau PJ, Ajji A, Rheol J. Influence of elastic properties on drop deformation and breakup in shear flow. J Rheol 1998;42(6).
[33] Mittal R, Dong H, Bozkurttas M, Najjar FM, Vargas A, von Loebbecke A. A versatile sharp interface immersed boundary method for incompressible flows with complex boundaries. J Comput Phys 2008;227(10):4825–52.
[34] Mittal R, Iaccarino G. Immersed boundary methods. Annu Rev Fluid Mech 2005;37:239–61.
[35] Muradoglu M, Gokaltun S. Implicit multigrid computations of buoyant drops through sinusoidal constrictions. J Appl Mech 2004;71(6):857–65.
[36] Muradoglu M, Kayaalp AD. An auxiliary grid method for computations of multiphase flows in complex geometries. J Comput Phys 2006;214(2):858–77.
[37] Nooranidoost M, Izbassarov D, Muradoglu M. Droplet formation in a flow focusing configuration: effects of viscoelasticity. Phys Fluids 2016;28(12). 123102.
[38] Olbricht WL. Pore-scale prototypes of multiphase flow in porous media. Annu Rev Fluid Mech 1996;28(1):187–213.
[39] Olbricht WL, Kung DM. The deformation and breakup of liquid drops in low Reynolds number flow through a capillary. Phys Fluids 1992;4(7):1347–54.
[40] Olbricht WL, Leal LG. The creeping motion of immiscible drops through a converging/diverging tube. J Fluid Mech 1983;134:329–55.
[41] Olgac U, Kayaalp AD, Muradoglu M. Buoyancy-driven motion and breakup of viscous drops in constricted capillaries. Int J Multiphase Flow 2006;32(9):1055–71.
[42] Shirai A. Modeling neutrophil transport in pulmonary capillaries. Respir Physiol Neurobiol 2008;163(1):158–65.
[43] Shirai A, Fujita R, Hayase T. Transit characteristics of a neutrophil passing through a circular constriction in a cylindrical capillary vessel (effect of mechanical properties of the cell and constriction geometry). JSME Int J Ser C 2002;45(4):974–80.
[44] Shirai A, Fujita R, Hayase T. Transit characteristics of a neutrophil passing through two moderate constrictions in a cylindrical capillary vessel. JSME Int J Ser C 2003;46(4):1198–207.
[45] Shirai A, Masuda S. Numerical simulation of passage of a neutrophil through a rectangular channel with a moderate constriction. PLoS ONE 2013;8(3). E59416.
[46] Squires TM, Quake SR. Microfluidics: fluid physics at the nanoliter scale. Rev Mod Phys 2005;77(3). 977.
[47] Stone HA, Stroock AD, Ajdari A. Engineering flows in small devices: microfluidics toward a lab-on-a-chip. Annu Rev Fluid Mech 2004;36:381–411.
[48] Tanner RI. A theory of die-swell. J Polym Sci A-2 1970;8(12):2067–78.
[49] Tryggvason G, Bunner B, Esmaeeli A, Juric D, Al-Rawahi N, Tauber W, et al. A front-tracking method for the computations of multiphase flow. J Comput Phys 2001;169(2):708–59.
[50] Tsai TM, Miksis MJ. Dynamics of a drop in a constricted capillary tube. J Fluid Mech 1994;274:197–217.
[51] Tseng YH, Ferziger JH. A ghost-cell immersed boundary method for flow in complex geometry. J Comput Phys 2003;192(2):593–623.
[52] Udaykumar HS, Kan HC, Shyy W, Tran-Son-Tay R. Multiphase dynamics in arbitrary geometries on fixed cartesian grids. J Comput Phys 1997;137(2):366–405.
[53] Unverdi SO, Tryggvason G. A front-tracking method for viscous, incompressible, multi-fluid flows. J Comput Phys 1992;100(1):25–37.
[54] Valvatne PH, Piri M, Lopez X, Blunt MJ. Predictive pore-scale modeling of single and multiphase flow. Transp Porous Med 2005;58(1):23–41.
[55] Wu H. Low Reynolds number dynamics of viscoelastic drop. Phd thesis. University of Virginia; 2008.
[56] Wu T, Feng JJ. Simulation of malaria-infected red blood cells in microfluidic channels: passage and blockage. Biomicrofluidics 2013;7(4). 044115.
[57] Yin B, Luo H. Numerical simulation of drops inside an asymmetric microchannel with protrusions. Comput Fluids 2013;82:14–28.
[58] Yue P, Feng JJ, Liu C, Shen J. Viscoelastic effects on drop deformation in steady shear. J Fluid Mech 2005;540:427–37.
[59] Zhou C, Yue P, Feng JJ. Simulation of neutrophil deformation and transport in capillaries using Newtonian and viscoelastic drop models. Ann Biomed Eng 2007;35(5):766–80.
[60] Zhou D, Yue P, Feng JJ. Viscoelastic effects on drop deformation in a converging pipe flow. J Rheol 2008;52(2):469–87.